Supporting Information

for

Upcycling Discarded Photovoltaic Backsheets to Polyvinylidene Fluoride Protective Layer for High-Performance Lithium-Ion Batteries

Hechen Sun[a,#], *Mingquan Tan*[a,#], *Xianggang Zhou*[a,#], *Bingwen Chen*[a], *Jiarui Zhang*[a], *Yingqi Li*[a,*], *Shanshan Xiao*[c,*], *Rui-Qi Yao*[a], *Xingyou Lang*[b,*], *Yang-Guang Li*[a,*], *Qing Jiang*[b]

[a] Key Laboratory of Polyoxometalate and Reticular Material Chemistry of Ministry of Education, Faculty of Chemistry, Northeast Normal University, Changchun, Jilin 130024, China

[b] Key Laboratory of Automobile Materials (Jilin University), Ministry of Education and School of Materials Science and Engineering, Jilin University, Changchun, 130022, China

[c] Laboratory of Building Energy-Saving Technology Engineering, College of Material Science and Engineering, Jilin Jianzhu University, Changchun 130118, China

[#] These authors contribute equally.

[*] Corresponding authors.

E-mail: liyq164@nenu.edu.cn (Y. Q. Li), xiaoshanshan@jlju.edu.cn (S. S. Xiao), xylang@jlu.edu.cn (X. Y. Lang) and liyg658@nenu.edu.cn (Y. -G. Li)

Keywords: CuO, polyvinylidene fluoride, recovery, photovoltaic backsheets, lithium-ion batteries

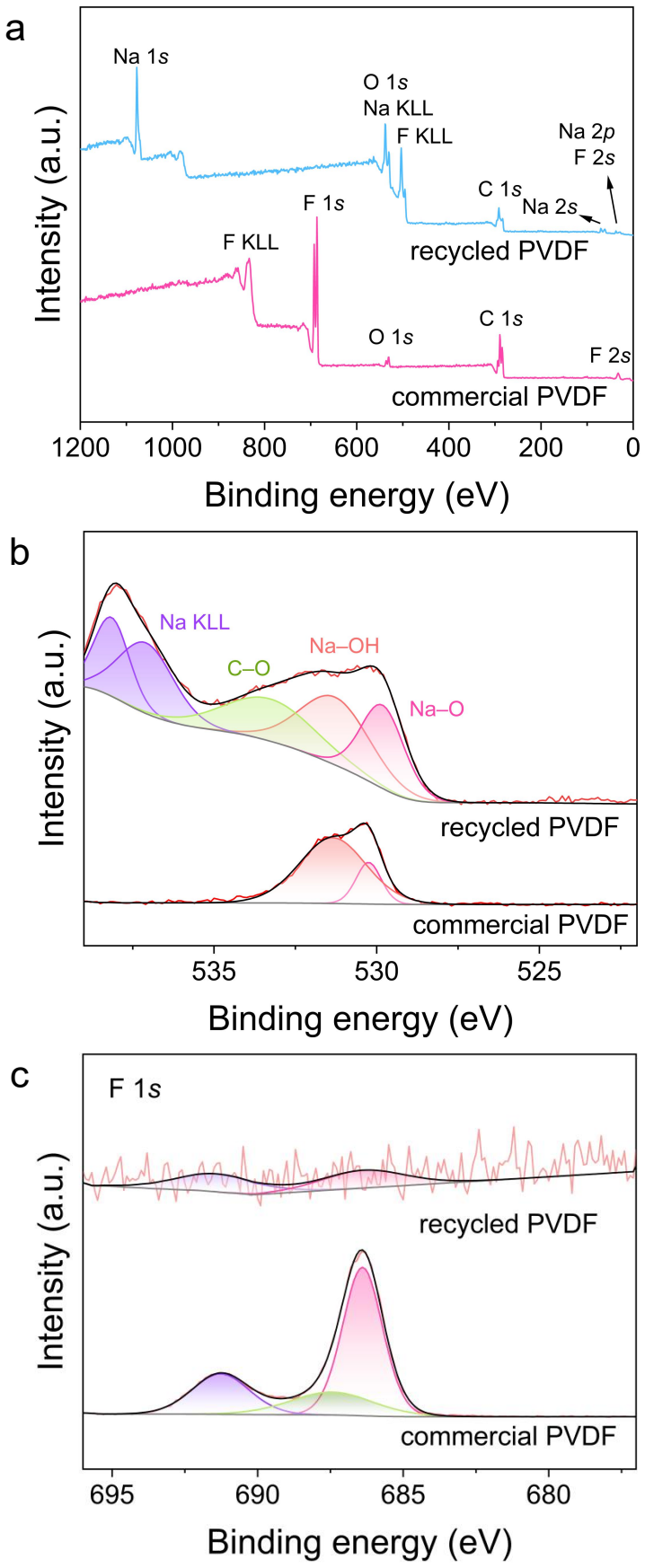

Figure S1. The XPS survey spectra of (a) full spectrum, (b) O 1*s* and (c) F 1*s* of recycled PVDF and commercial PVDF.

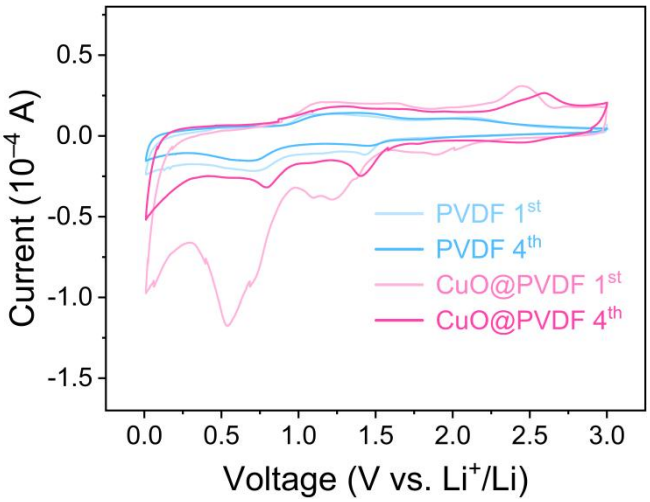

Figure S2. CV curves of the 1st and 4th cycles for pure PVDF and CuO@PVDF anodes at a scan rate of 0.2 mV s^{-1}.

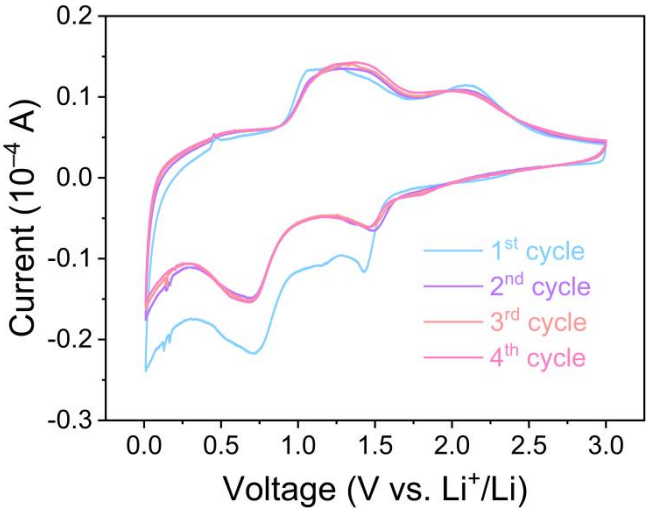

Figure S3. CV curves of the first four cycles for pure PVDF anode at a scan rate of 0.2 mV s^{-1}.

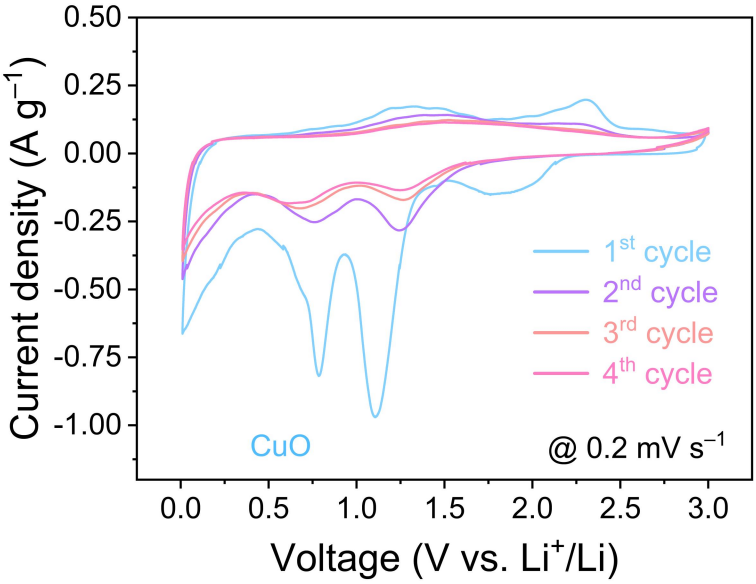

Figure S4. The first four CV cycles of CuO anode with scan rates of 0.2 mV s^{-1}.

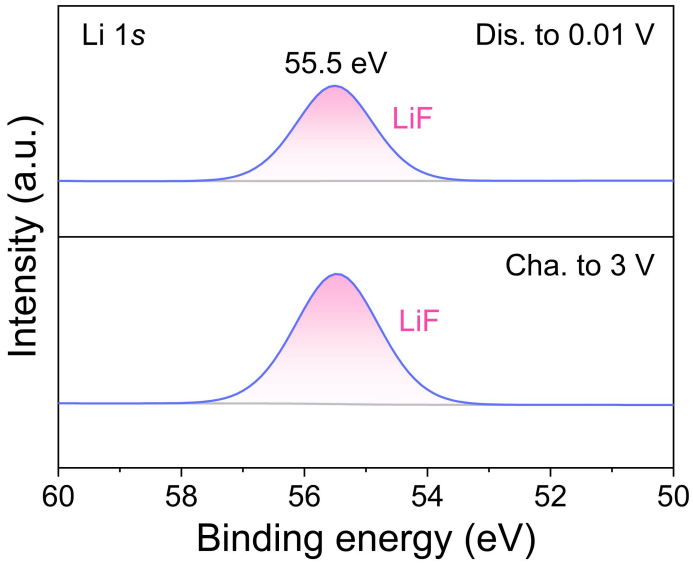

Figure S5. The XPS survey spectra of Li 1*s* after fully discharged (0.01 V) and charged (3 V) states of CuO@PVDF electrode.

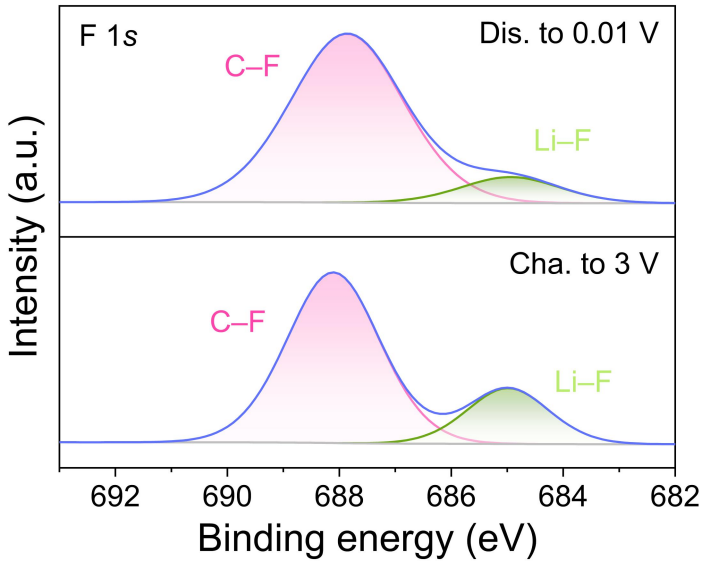

Figure S6. The XPS survey spectra of F 1*s* after fully discharged (0.01 V) and charged (3 V) states of CuO@PVDF electrode.

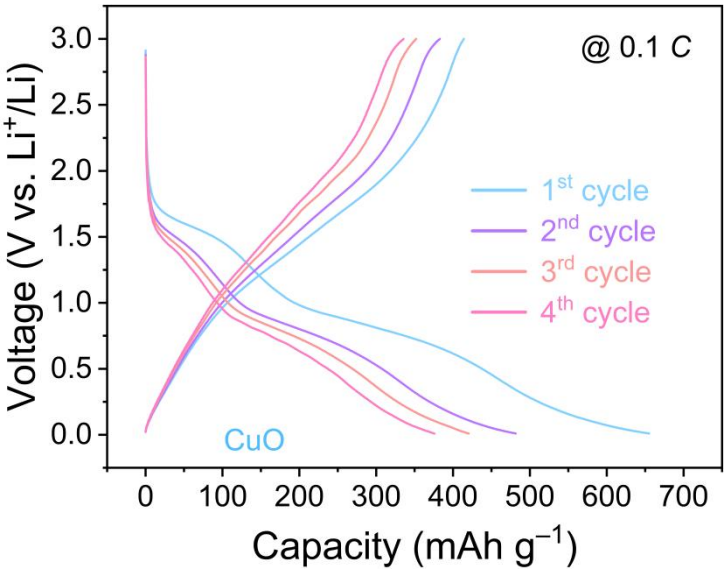

Figure S7. GCD curves for the first four cycles of the bare CuO anode at a current density of 0.1 *C*.

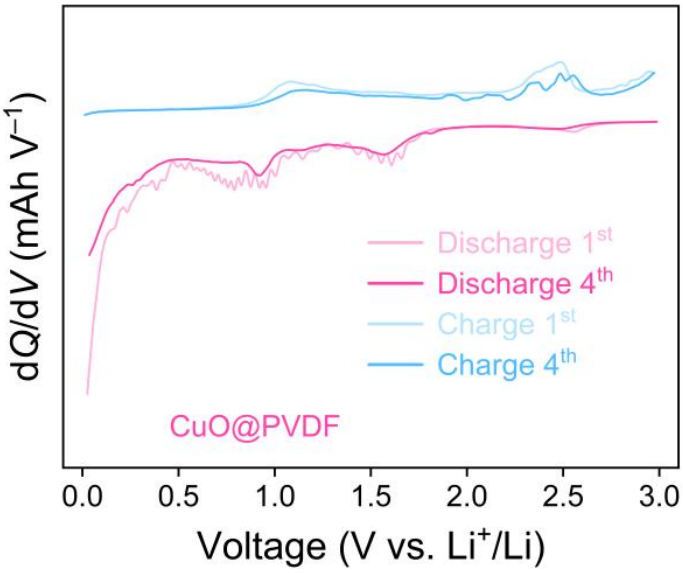

Figure S8. Corresponding dQ/dV curves for the 1st and 4th cycles of the CuO@PVDF anode at the voltage range of 0.01-3 V at a current density of 0.1 C.

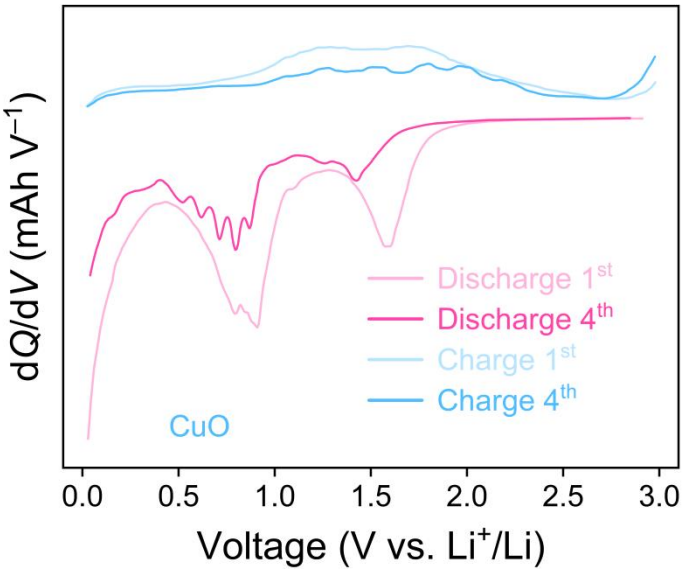

Figure S9. Corresponding dQ/dV curves for the 1st and 4th cycles of the bare CuO anode at the voltage range of 0.01-3 V at a current density of 0.1 C.

Table S1. Comparison of lithium storage performance of different TMO-based electrode materials.

Electrode materials	Capacity (mAh g^{-1})	Reference
CuO/RG	647 (0.37 A g^{-1})	[45]
Cu/CuO/Cu_2S	551 (0.15 A g^{-1})	[46]
CuO/MXene	436.4 (0.5 A g^{-1})	[47]
NiO@CuO/CNT	905 (0.2 A g^{-1})	[48]
CuO@Cu/g-C_3N_4	726 (0.67 A g^{-1})	[49]
Cu/Cu_2O@Ppy	509 (0.1 A g^{-1})	[50]
Hollow CuO@C	630 (0.1 A g^{-1})	[51]
RD-CuO@Cu	826.2 (0.1 A g^{-1})	[52]
Co_3O_4@CuO@GQDs	921 (0.1 A g^{-1})	[53]
10ZnO-CuO	246 (0.5 A g^{-1})	[54]
0.5-CuO/Fe_2O_3 NSs	~1020 (0.1 A g^{-1})	[55]
$Ti_3C_2O_x$/FeOOH/Fe_3O_4	894.6 (0.1 A g^{-1})	[56]
Fe_3O_4/FeS@S-MX	746.6 (0.1 A g^{-1})	[57]
CuO@PVDF	**1180.6 (0.125 A g^{-1})** **747 (0.5 A g^{-1})** **573 (1 A g^{-1})**	**This Work**

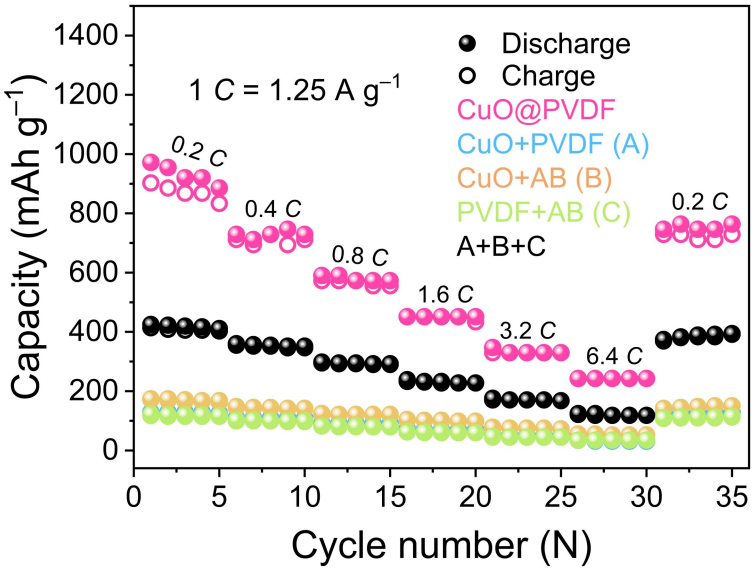

Figure S10. Rate performance of CuO@PVDF, CuO+PVDF (A), CuO+AB (B), PVDF+AB (C) anodes, and the sum specific capacity of the three control sample (A+B+C).

The rate performances of CuO@PVDF, CuO+PVDF (A), CuO+AB (B), PVDF+AB (C), and the sum specific capacity of the three control sample (A+B+C) were shown in **Figure S10**. At the same current density, CuO@PVDF with CuO:PVDF:AB = 6:2:2 exhibited higher specific capacities than the control samples, which indicated that in CuO@PVDF, CuO provided the capacity from the reaction between CuO and Li^+, PVDF buffered the volume expansion of CuO during cycles, and acetylene black increased the conductivity of the materials. The synergistic addition of PVDF and AB significantly strengthen the electrochemical performance of CuO.

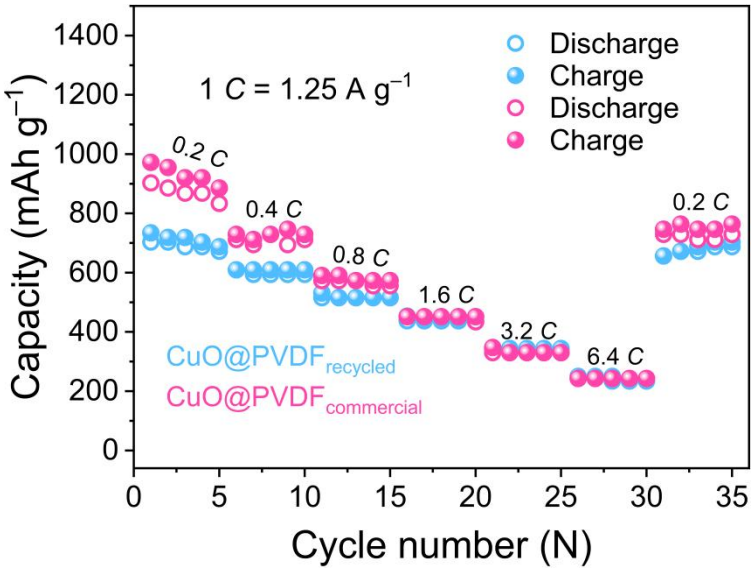

Figure S11. Rate performance of CuO@PVDF (recycled) and CuO@PVDF (commercial) .

The two CuO@PVDF anodes exhibited similar performance, indicating that both recycled PVDF and commercial PVDF provide comparable protection for CuO.

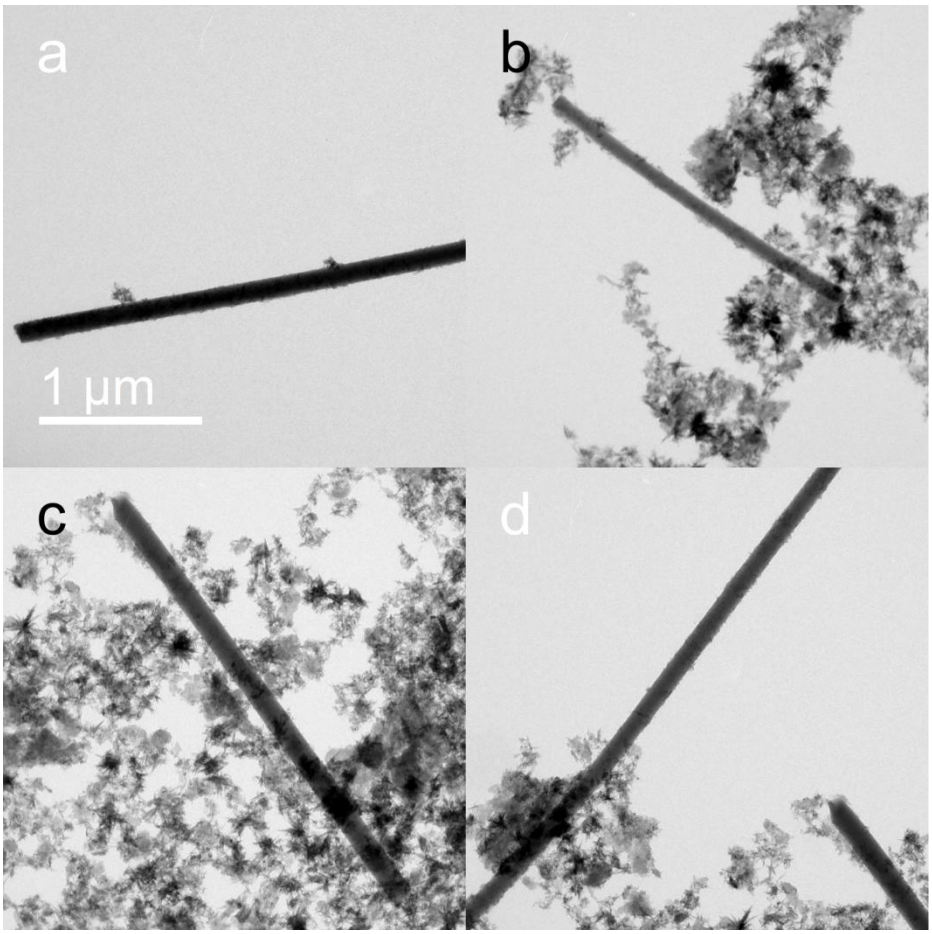

Figure S12. TEM images of CuO@PVDF after 1600 cycles at a current density of 1 *C*.

As shown in Figure S12, CuO@PVDF retained its original strip-like structure as observed before cycling, with no signs of damage, fracture, pulverization or deformation caused by severe volume expansion. These findings demonstrate that PVDF effectively buffered the volume changes of CuO. In comparison, bare CuO anode exhibited a serious capacity decay in both rate and cycle performance, indicating that CuO without PVDF protection suffer from volume expansion.

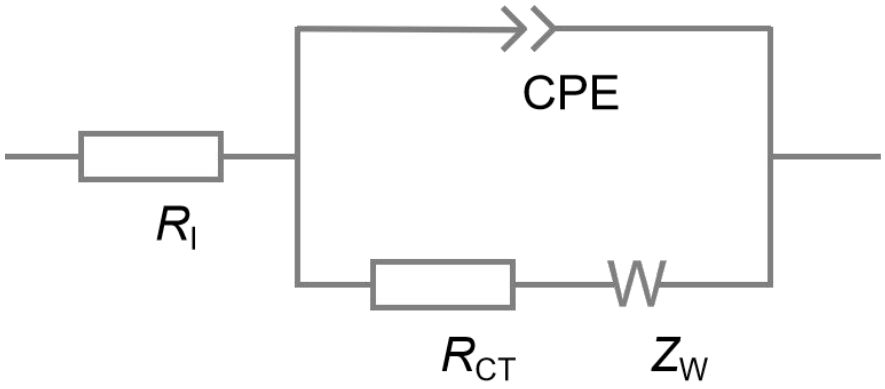

Figure S13. The electrical equivalent circuit diagram for the electrochemical impedance spectra (EIS) of bare CuO and CuO@PVDF hybrid electrodes for LIBs.

Table S2. Comparison of the R_I and R_{CT} of bare CuO and CuO@PVDF hybrid electrodes before and after cycles.

		CuO	CuO@PVDF
before	R_I (Ω)	7.33	6.16
	R_{CT} (Ω)	254.6	406
after	R_I (Ω)	3.01	1.93
	R_{CT} (Ω)	233.2	323.2

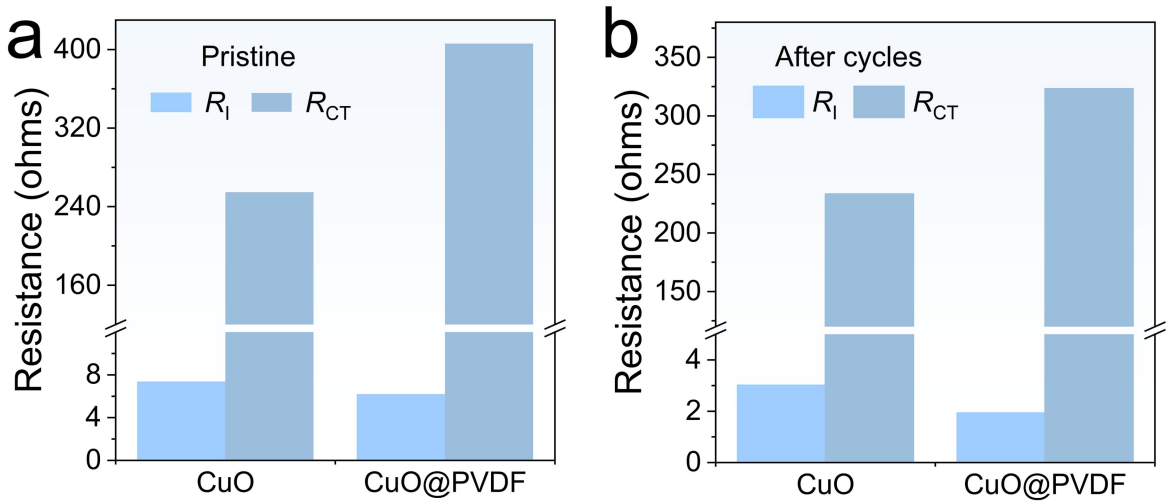

Figure S14. Comparison of the intrinsic resistance (R_I) and the charge transfer resistance (R_{CT}) of bare CuO and CuO@PVDF hybrid electrodes (a) before and (b) after cycles.

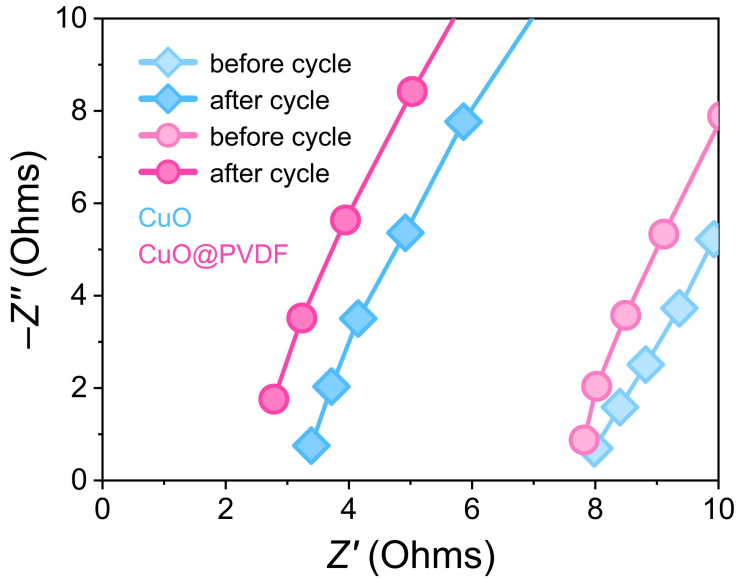

Figure S15. EIS measurements of bare CuO and CuO@PVDF anodes at high frequency range.

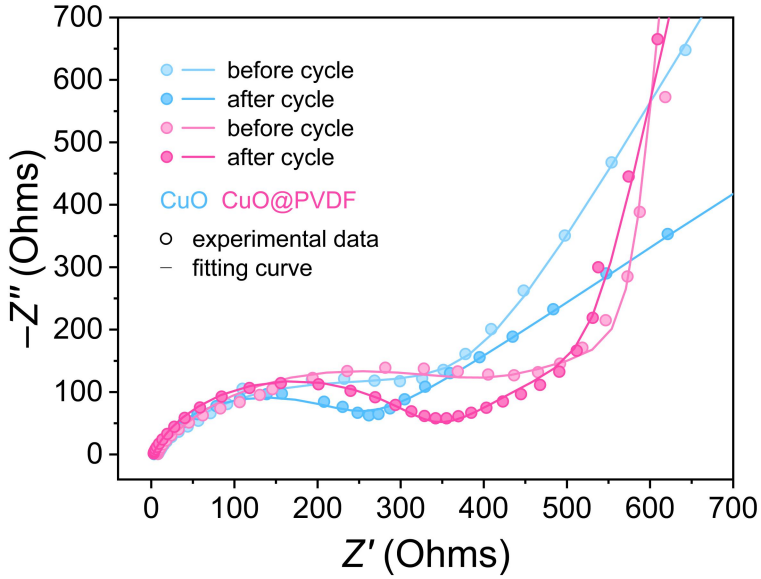

Figure S16. EIS measurements of bare CuO and CuO@PVDF anodes and fitting curve.

R_I denotes intrinsic resistance (solution resistance R_S or ohmic resistance R_Ω), R_I in the battery system including electrode materials and current collectors. In the Nyquist plot, it corresponds to the first intersection point between the curve and the real axis in the highest frequency region. R_{CT} denotes charge transfer resistance, which indicates the difficulty of

electrochemical reactions occurring at the electrode/electrolyte interface. It reflects the driving force required for lithium ions to overcome electrochemical polarization during insertion/extraction from the electrode material. Key influencing factors include temperature, state of charge, and the intrinsic reaction kinetics of the electrode material. In a Nyquist plot, R_{CT} corresponds to the diameter of the semicircle in the intermediate frequency region. Z_W denotes Warburg impedance (open), *i.e.* model of finite diffusion layer. It represents the solid-phase diffusion process. Specifically, it refers to the diffusion resistance of lithium ions within the electrode active material particles due to concentration gradients. It corresponds to a diagonal line in the low frequency region. CPE denotes Constant Phase Element. In practical electrochemical systems, the behavior of the double electric layer often deviates from ideal capacitance due to electrode surface roughness, porosity, uneven current distribution, and adsorption effects. The CPE is a component used to describe this "non-ideal capacitance" behavior. It represents the dispersion effect of the double-layer capacitance at the electrode/electrolyte interface. CPE is typically performed alongside R_{CT} to simulate the flattened semicircle in the intermediate frequency range.

Frequency window: 10 mHz ~ 100 kHz.

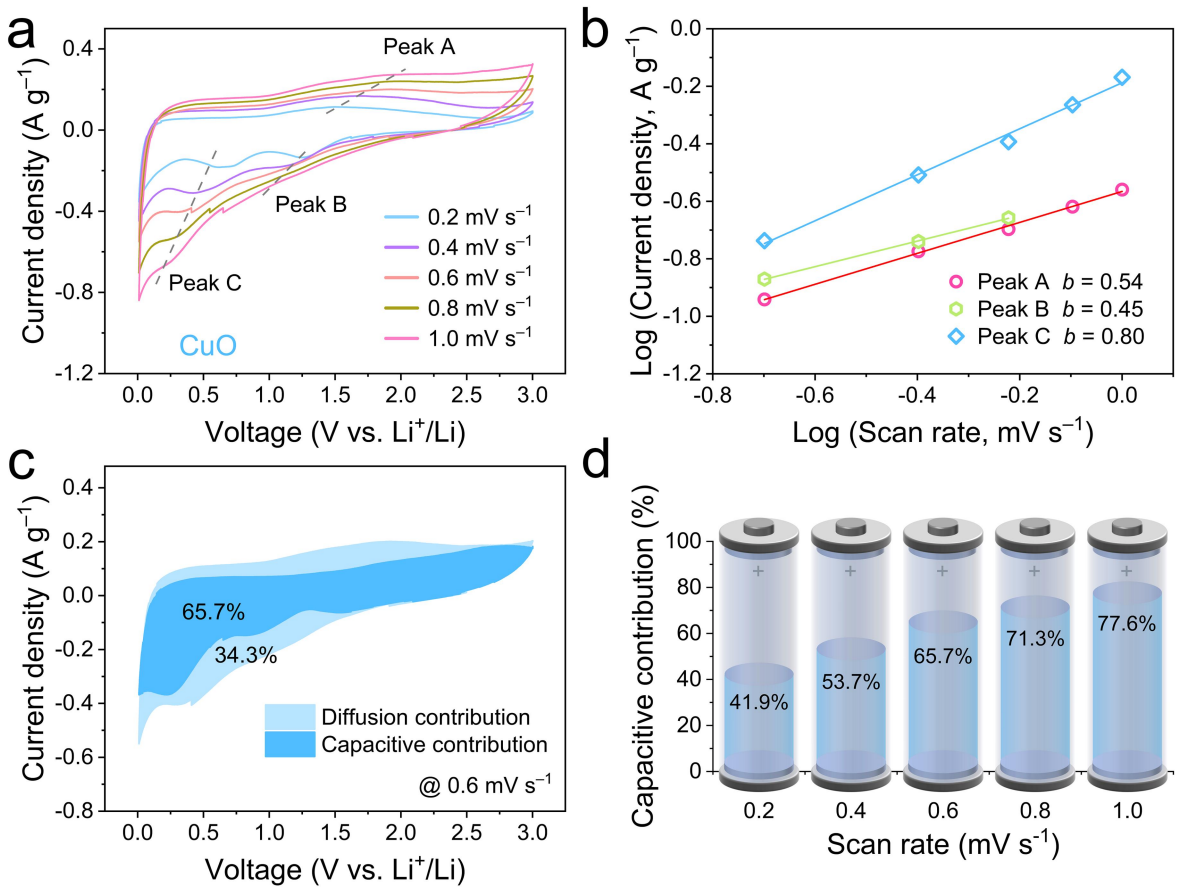

Figure S17. (a) CV curves for the CuO anode at 0.2, 0.4, 0.6, 0.8 and 1.0 mV s^{-1} over a voltage window of 0.01-3 V. (b) Correspondence between the logarithm of the peak current density and the logarithm of the scan rate. (c) Capacitive storage contribution of CuO anode at 0.6 mV s^{-1}. (d) Capacitive contribution of CuO anode at various scan rates.

References

45. K. Chen, H. Yu, M. Huang, Z. Wang, Y. Li, L. Zhou, L. Yang, Y. Feng, L. Chen, L. Wang, L. Wang, C. Xu, P. Shao and X. Luo, *Green Chem.*, 2024, **26**, 6634–6642.
46. M. Wei, Q. Zhang, L. Huang, Z. Xue, Q. Gao, X. Cai, S. Zhang, Y. Fang, F. Peng, T. Yuan and S. Yang, *Nano Lett.*, 2024, **24**, 10827–10833.
47. D. Zhang, R. Kang, G. Zhang, R. Yang, W. Liu, H. Qin, L. Miao and F. Dang. *ACS Appl. Nano Mater.*, 2023, **6**, 21652–21662.
48. J. Wang, X. Guo, X. Du, J. Liang, J. Wu, G. Zhao, X. Li, S. Gui, F. Zheng, J. Zhao, C. Xu, D. Wang, H. Yang, B. Zhang and Y. Zhu, *Energy Storage Mater.*, 2022, **51**, 11–18.
49. H. Mohamed, C. Li, L. Wu, W. Shi, W. Dong, J. Liu, Z. Hu, L. Chen, Y. Li and B. Su, *Chem. Eng. J.*, 2021, **407**, 126941.
50. Y. Wang, L. Cao, J. Li, L. Kou, J. Huang, Y. Feng and S. Chen, *Chem. Eng. J.*, 2020, **391**, 123597.
51. Y. Dong, X. Jiang, J. Mo, Y. Zhou and J. Zhou, *Chem. Eng. J.*, 2020, **381**, 122614.
52. B. Liu, J. Zhang, X. Li, Y. Li, T. Xu, H. Huang, B. Zhang, J. Yuan, Y. Cheng, X. Chen, H. Zeng and Y. Wu. *Nano Res.*, 2025, **18**, 94908193.
53. M. Wu, H. Chen, L. Lv and Y. Wang, *Chem. Eng. J.*, 2019, **373**, 985–994.
54. Y. Zhang, Y. Xu, Y. Ji, X. Wang, J. Li, H. Liu, D. Wang, Z. Zhong, Y. Bando and F. Su, *Energy Storage Mater.*, 2019, **17**, 242–252.
55. Y. Wang, Q. Zhuang, Y. Li, Y. Hu, Y. Liu, Q. Zhang, L. Shi, C. He, X. Zheng and S. Yu, *Nano Res.*, 2022, **15**, 5064–5071.
56. T. Ruan, J. Xu, N. Fang, S. Lu, J. Zhou, X. Yin and R. Li, *Adv. Funct. Mater.*, 2024, **35**, 2418307.
57. T. T. Ruan, B. Wang, Y. B. Yang, X. Zhang, R. S. Song, Y. Ning, Z. B. Wang, H. J. Yu, Y. Zhou, D. L. Wang, H. K. Liu and S. X. Dou, *Adv. Mater.*, 2020, **32**, 2000151.